Supplemental Material for:

Electron and X-Ray Focused Beam Induced Crosslinking in Liquids: Toward Rapid Continuous 3D Nanoprinting and Interfacing using Soft Materials

Tanya Gupta[1,2], Evgheni Strelcov[1,2], Glenn Holland[1], Joshua Schumacher[1], Yang Yang[1], Mandy B. Esch[1], Vladimir Aksyuk[1], Patrick Zeller[3], Matteo Amati[3], Luca Gregoratti[3], and Andrei Kolmakov[1]*

[1] NIST, Gaithersburg, MD 20899, USA;
[2] Maryland NanoCenter, University of Maryland, College Park, MD 20742, USA;
[3]Elettra Sincrotrone, Trieste 34012, Italy

Height estimation

The dimensions of the obtained features were measured using various techniques, including optical Profilometry (Figure S1 a, d), SEM (Figure S1 b, e, f) and AFM (Figure S1 c). Depending on the shape and size of the features different methods were found suitable.

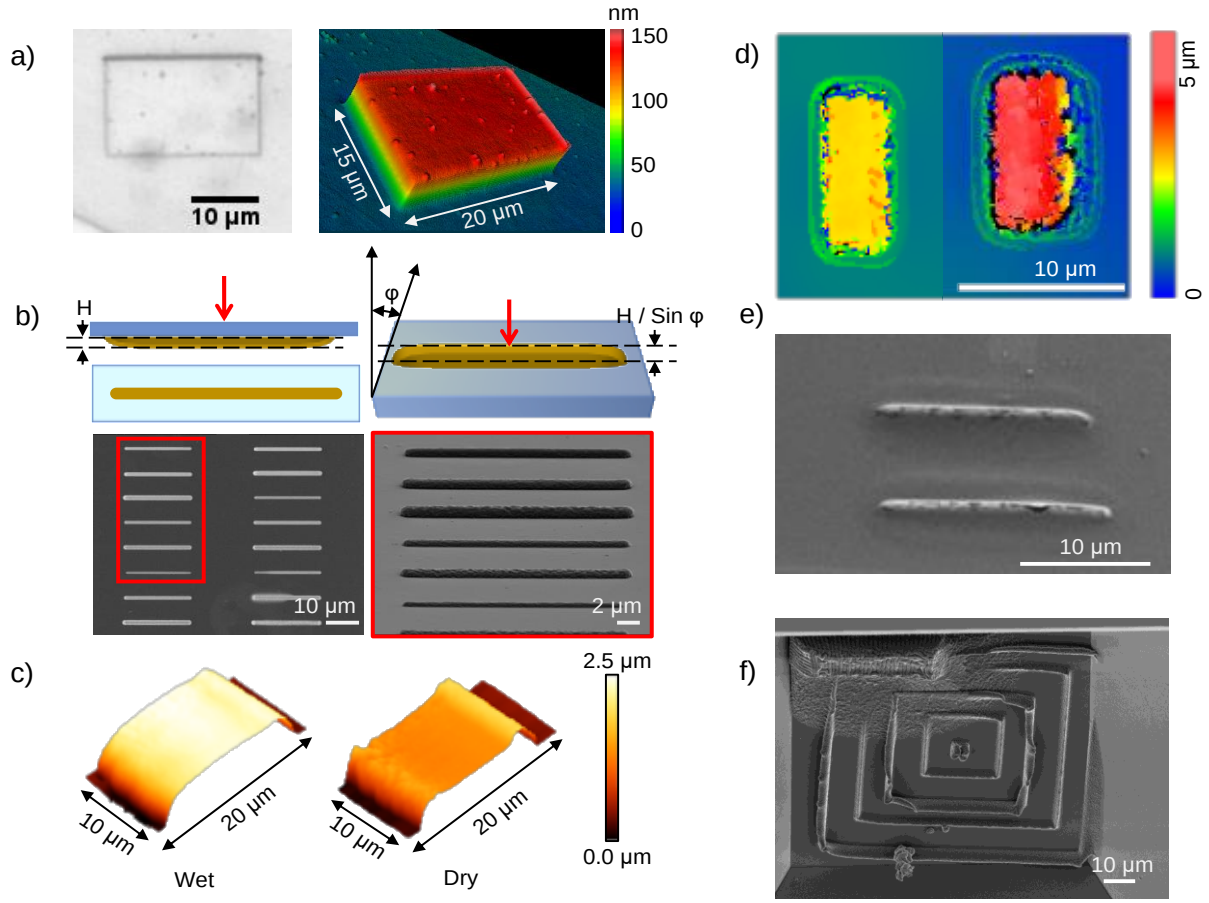

Figure S1 Different methods of height estimation are shown for a), b), c) electron crosslinked samples and d), e), f) X-ray crosslinked samples. a) Profilometry: (left) optical image, (right) 3D structure of the hydrogel formed at 3 kV. b) SEM: (left) image of thin lines taken through the membrane; (right) the same sample was placed upside down and tilted to view projection of the cross-section. Height was estimated based on the angle of tilt. c) AFM of hydrogel done in a hydrated state (left) and same feature done in a dry environment (right). d) Profilometry of 536 eV X-ray sample (left) and 526 eV X-ray sample (right). e) SEM of X-ray lines formed at 526 eV. f) SEM of the labyrinth-like structure formed by squares alternating from 526 eV to 536 eV from the center out.

Samples with larger dimensions were quantified using profilometry. For laterally thin samples, SEM was found to be most suitable. The sample was mounted on a tilted stage facing the electron beam. The projected height of the sample can be measured and used to calculate the actual height based on the tilt angle as shown for electron samples in Figure S1 b. For vertically thin features generated using low electron beam energy, AFM (Figure S1 c) was found to be most accurate for height estimation. Similar height estimations were done for X-ray crosslinked samples as shown in Figure S1 d, e, f. For consistency, all measurements were done after exposing the sample to vacuum.

Since these hydrogels have a high-volume fraction of water, they shrink when exposed to air or vacuum. This is deduced by measuring the shrinkage of macro-sized UV cured hydrogels with time using an optical microscope, as shown in Figure S2 a. UV cured samples shrink to 20% of their original wet size. However, there can be differences in the water content of the UV cured samples and the electron beam cured samples depending on the density of crosslinking. In order to estimate the original dimension of electron beam cured wet hydrogel, AFM was done in the hydrated state in a liquid environment and then post drying on the same feature. Results, shown in Figure S2 b, suggest an average shrinkage of 50% ± 20% on vacuum drying. This is significantly less when compared to shrinkage fraction in UV cured samples (80%) suggesting

differences in the curing mechanism of the two techniques. The difference between these two techniques can be seen in the SEM images in Figure S2 c, where the UV cured samples exhibits rougher morphology upon drying indicative of a more porous structure. For comparison SEM image of X-ray crosslinked sample is also shown, reflecting patterns which are intermediate in size, between the UV and electron crosslinked samples. We conclude that the original dimensions of the as-prepared hydrated hydrogel *via* electron beam and X-ray samples are therefore approximately twice and two-four times as large compared to the dry values, respectively. All dimensions shown in the main text Figure 2 are from dry samples.

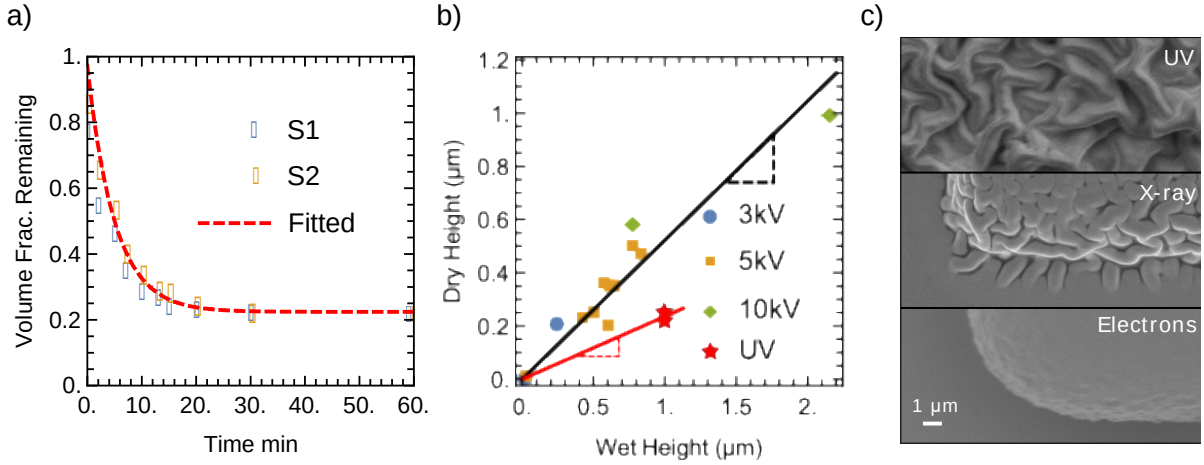

Figure S2 Effect of drying on UV cured and E-beam cured samples. a) Volume Fraction remaining of UV cured samples S1 and S2 as a function of time b) dry height *vs.* wet height of different samples to estimate the dry fraction. Average Dry fraction for e-beam samples 0.52 (black line) and for UV cured samples is 0.2 (red line). C) SEM image of UV cured, X-ray cured, and electron beam cured samples at similar settings and magnification after drying.

A correction factor of 2 is therefore multiplied to the dry height of the electron beam samples to obtain the wet height.

X-ray Dose Estimation

Intensity attenuation of X-rays with depth can be calculated using Beer-Lamberts law:

$$N = N_0 \exp(-\mu d) \tag{1}$$

here N_0 is the photon flux per unit area at the surface, $\frac{1}{\mu}$ is the attenuation length and d is the depth. Dose per unit mass can then be calculated as

$$-\frac{1}{\rho}\frac{\partial(N\,h\nu)}{\partial d} = \frac{\mu N_0 h\nu}{\rho}\exp(-\mu d) \tag{2}$$

here ρ is the density of the interacting media and $h\nu$ is the photon energy. Beam shape at the sample was known to be Gaussian with FWHM of 150 nm. Measurements from photodiodes were calibrated to obtain the total photon flux on the sample. From the beam shape and total flux, N_0 was calculated by averaging over the pixel area (same as step size).

Electron Dose Estimation

The spatial distribution of energy is computed using Monte-Carlo simulations[1], where a primary beam of known energy is allowed to interact with a stack of 50 nm Silicon Nitride membrane and bulk water. The electrons are allowed to experience elastic and inelastic collisions in a cascade-like process as they travel until they reach threshold energy and thermalize. The elastic interactions were treated as discrete events using Motts cross-section, whereas the inelastic events were approximated based on the mean energy loss model by Joy & Luo [2]. Figure S3a shows the trajectory of electrons with the color denoting the energy of electrons for 5 keV primary beam. The corresponding energy deposited distribution into the water is shown in Figure S3 b.

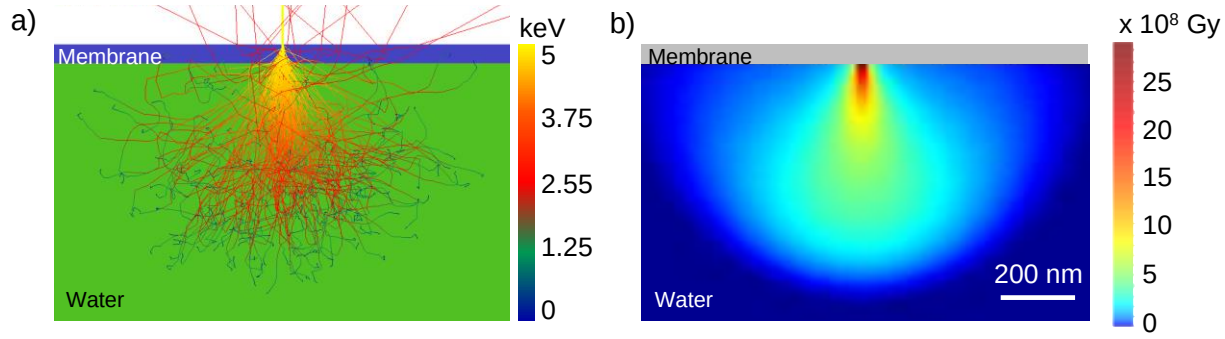

Figure S3 Results from Monte-Carlo simulation generated by simulating 625000 electrons, for a 5 nm beam diameter at 5 keV primary beam energy. a) The trajectory of electrons, with color denoting the energy of the electron. b) spatial distribution of the energy deposited distribution in water.

Monte Carlo simulations, indicate fast decrease of the dose with radial distance from the point of incidence of the primary beam. Since most experiments are done in scanning mode, literature typically reports the dose at the surface, averaged over the pixel area, in units of e^-/nm^2, referred to as c_p^o , or in units of Gy (J/kg), referred to as φ_p^o in the main text. The dose can be expressed as

$$c_p^o = \frac{I_B \, \tau_D \, n}{A_p} \tag{3}$$

Where I_B is the beam current in e^-/ sec, A_p is the pixel area in nm^2, τ_D is the dwell-time per scan in seconds and n is the number of scans. Unless otherwise mentioned, in this study the pixel size is 100 nm x 100 nm and the number of scans is 1.

This can be further converted into pixel averaged surface dose in Gy (J/kg) using conversion relation:

$$\varphi_p^o \left(Gy \; or \frac{J}{kg} \right) = S_P \left(MeV \frac{cm^2}{g} \right) \left(\frac{1.6 * 10^{-19} * 10^6}{10^{-3}} \right) * c_p^o \left(\frac{\#\; of \; electrons}{nm^2} \right) \left(10^{14} \frac{nm^2}{cm^2} \right) \tag{4}$$

here S_P is the density normalized stopping power for electrons, which in turn is a function of the energy of electrons. For example, once we know the c_p^o for the set of parameters (1nA, 1 ms 100nm x 100nm), for known energy of primary beam (say E = 3 keV, with the S_P of electrons in water in 56.21 MeV cm^2/g), φ_p^o is 5.61 x 10^8 Gy.

Table S1 A few examples of the dose values used for PEG crosslinking and electron microscopy of microorganisms.

Radiation & parameters	**Crosslinking dose & conversion**	**Comment**	**Reference**

X-rays ~12 keV	~ 3 10^7 Gy	Pegilation of Au NP in solution	[3]
Electrons 10 keV 20-100 pA	~ 0.1 C/m^2= 1 e/nm^2	Dry PEG 6800	[4]
50 eV electrons	~ 5·10^3 e/nm^2	Carbonization of PEG	[5]
	Cells viability dose		
TEM	5×10^{-3} e^-/nm^2 at 100 kV	Reproductive death of E. coli	[6]
TEM	37 e^-/nm^2,	Minimum dose required for high resolution (5 nm) imaging of bio specimen (note that this is larger than viability dose)	[6] pp 468– 480
TEM	6.2×10^{-4} e^-/nm^2	colony-forming properties of *E. coli*	Isaacson, M. S. Specimen Damage in the Electron Microscope. In [7] pp 43– 44
TEM	1 to 80 e^-/nm^2	E.coli increasingly compromised after ca 30 e/nm^2	[8]
ESEM 30 kV	10^3 to 10^5 e^-/ nm^2	fixed COS7 fibroblasts, can be kept undamaged	[9]
Soft X rays 385 eV	1 ph/ nm^2 (~25 kGy)	Myofibrils contraction stops	[10]

For clarity and direct comparison with literature values, we report the c_p^o and φ_p^o value for various instances in the main text. For more accurate estimations where the spatial distribution is needed (for example, as inputs into the Kinetic model below), we use Monte Carlo simulations.
A systematic discrepancy is observed between the experimental height and the one predicted from Monte-Carlo simulations, as shown in Figure S4

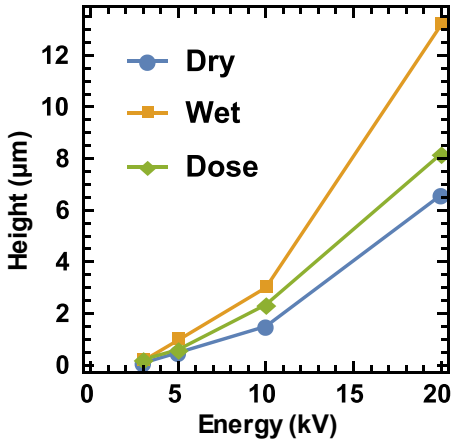

Figure S4 Height *vs.* Energy of Primary beam for parameters of 400 pA current and 1 ms dwell time for the electron beam. (blue) dry height measured from experiments. (orange) wet height estimated assuming 50% shrinkage. (green) Height estimated assuming critical crosslinking dose of 10^6 Gy.

We hypothesize that this discrepancy is a result of diffusion of radiolytic species which contributes to an increase in the size of the experimental features. A kinetic model, taking into account the effect of diffusion, is therefore formulated and presented here to bolster this theory.

Kinetic Model

A kinetic model involving generation, reaction, and diffusion of the radiolytic species is built for application to liquids in SEM. This is based on a prior model by Schneider *et al.* that was developed for TEM[11, 12] . The model is adapted to account for the highly non-uniform spatial dose deposition in case of SEM, by coupling it with Monte-Carlo simulations. The model framework comprises of a coupled differential equation (Eqn. 5) based on transport of dilute species for each primary and secondary radiolytic species. All parameters including the rate constants and diffusion coefficients can be found elsewhere [12].
Briefly, the model can be described as follows. Energy is deposited by the electron beam into the hydrogel solution. The calculated 2D axisymmetric energy distribution, shown in Figure S3 b, is fed as input into the kinetic model. This energy dose acts as a source for generation of primary radiolytic species *via* breakdown of water ($e_h^-, H, H_2, OH, H_2O_2, HO_2, H^+, OH^-$) which in turn react to produce secondary species ($HO_2^-, HO_3, O_2, O_2^-, O_3, O_3^-, O^-$). Empirical G-values[11, 12] for primary radiolytic species (

Table S) are used to correlate dose and the concentration of radiolytic species produced (Eq. 6). G-values for secondary species is 0. All species are allowed to react and diffuse until they reach a steady state (~1 ms).

Table S2 G-values for primary radiolytic species

Species	**G-values (molecules/100 eV)**
e_h^-	3.47
H	1.00
H_2	0.17
OH	3.63
H_2O_2	0.47
HO_2	0.08
H^+	4.42
OH^-	0.95

$$\frac{dC_i(r,z)}{dt} = D_i\,\nabla^2 C_i(r,z) + \sum_{j,k\neq i} k_{jk}\,C_j(r,z)\,C_k(r,z) - \sum_{l} k_{il}\,C_i(r,z)C_l(r,z) + \mathrm{S_i}(r,z) \qquad (5)$$

$$S_i(r,z) = \varphi_B(r,z)G_i \qquad (6)$$

Where (r,z) are cylindrical coordinates, axisymmetric across the vertical axis along the line of incidence of the Primary beam. C_i is the concentration, D_i is the diffusion constant, $\mathrm{S_i}$ is the source term, φ_B is the energy density deposited and G_i is the G-value of the i^{th} species.

Imaging of composite gels with SEM

For many applications, it is important to image the encapsulated particles inside the gel with high spatial resolution. Figure S5 depicts the SEM image of 50 nm Au nanoparticles entrapped inside the crosslinked hydrogel matrix collected with the detector sensitive to fast backscattered electrons (BSE). In this SEM imaging mode, the contrast of the objects is determined by the difference of the atomic numbers (Z) of the nanoparticle and matrix material as well as on the depth at which the electrons are collected. In the SEM

image Au particles with much larger effective Z compared to hydrogel matrix appear brighter, and both: their signal strength and the resolution wanes with the depth of the nanoparticle inside the gel (Figure S5). To evaluate the feasible imaging depth for hydrogel embedded objects we conducted MC simulation of the BSE images of heterogeneous and compared them with the experimental data (Figure S5). As can be seen, SEM can be used to probe nanoparticles as deep as a few hundred nanometers using a 20kV beam energy with resolution still better compared to conventional optical microscopy.

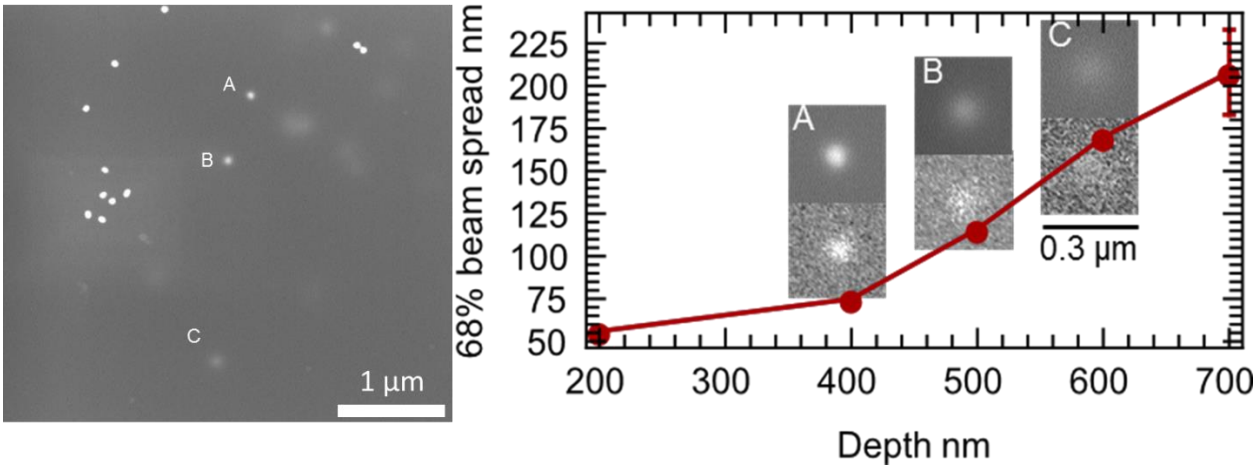

Figure S5 (Left) SEM image (E_b=20 keV) of embedded Au nanoparticles collected with backscattered electrons. The observed effective diameters increase, and BSE signal reduction is due to the different depth of embedded nanoparticles. (Right) MC simulated diameter of 50 nm nanoparticles as a function of the particle depth. Insets are comparisons experimentally observed and MC simulated SEM images

Raman Analysis

Raman analysis was done to validate the chemical effect of the curing process. Raman spectra of dried PEGDA correlates well with the previous studies[13, 14] showing C-H-C bending peak at 1470 cm^{-1} (Figure S6 peak b) and C=C peaks at 1640 and 1410 cm^{-1} (Figure S6 peaks a, d and e). Peaks at 1600 and 1676 cm^{-1} are from the initiator Irgacure 2959 as indicated by their appearance only after the initiator is added. Literature suggests 1600 cm^{-1} peak corresponds to C=C stretching in an aromatic ring. Post-exposure to electron beam the C=C stretching peaks of PEGDA and unidentified peak at 1705 cm^{-1} are reduced (peaks a, d and e in S6), supporting crosslinking induced by a breakdown of pi bonds. The spectra in the left and right panels have been collected in dry and hydrated conditions and using different spectrometers. No major differences can be observed except the relative intensity of water (ca. 2900-3900 cm^{-1}) band. For spectrum collection under wet conditions a small droplet of PEGDA solution was drop casted near a hydrated e-patterned patch (see inset).

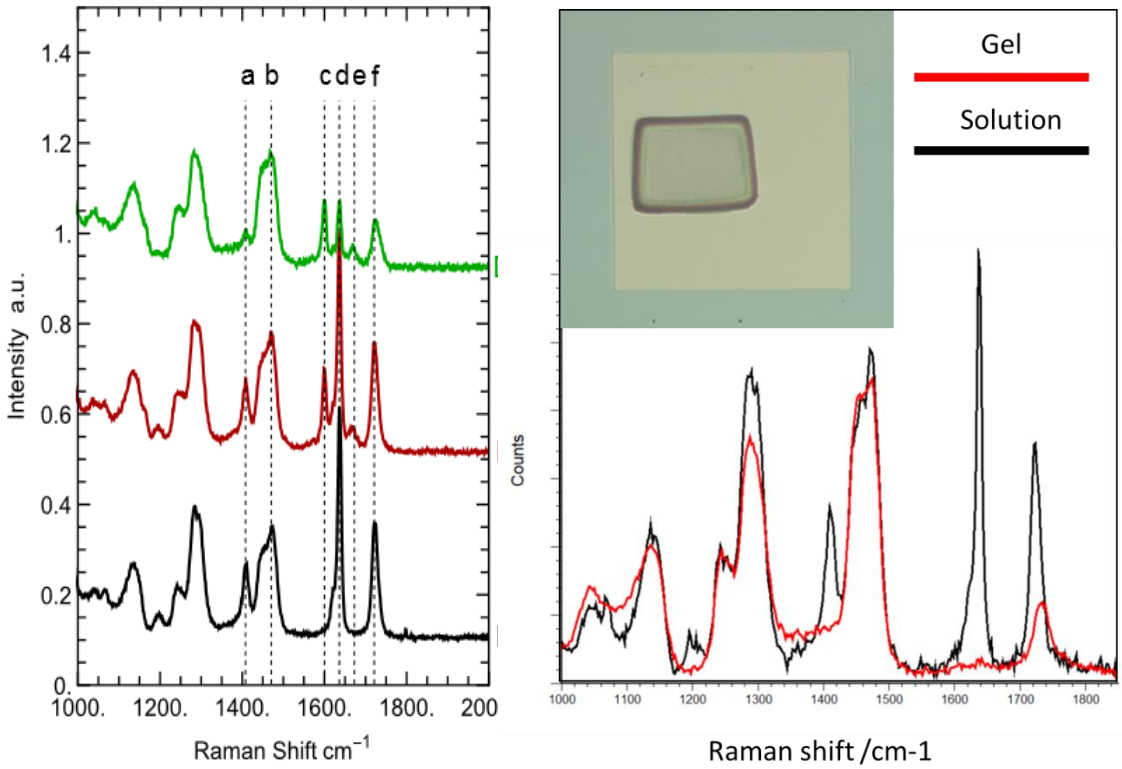

Figure S6. Left panel: Raman spectra for dried PEGDA sample excited using 532 nm laser, *(black)* without initiator before e-beam exposure, *(red)* with initiator before e-beam exposure, *(green)* with initiator after e-beam exposure. All spectra are normalized w.r.t. peak b representing C-H-C bending. Peaks a, c, d, e, and f are the ones which are useful in interpreting the chemical structure and its changes on exposure to e-beam and are discussed in the text. Right panel: Raman spectra collected under hydrated conditions from the e-beam gelated PEGDA pad (red curve) and PEGDA solution (black curve).

Plasmonic sensor measurements

Humidity-dependent optical spectroscopy measurements reported in Fig. 4 b, c of the main text were performed using commercially-available microscope, spectrometer and CCD camera. Spectra were collected from a small nanoparticle agglomerate in dark field mode in the wavelength range from 400 nm to 750 nm using 150 Gr/mm grating blazed at 800 nm. The sample was enclosed in a commercially available environmental cell with an optical window. Relative humidity of argon gas inside the cell was controlled using custom-made humidifier (Fig. S7) consisting of two flow meters and a bubbler flask. The ratio between the dry gas flow and the gas flow through the bubbler (100% relative humidity) determined the final gas humidity the sample was exposed to.

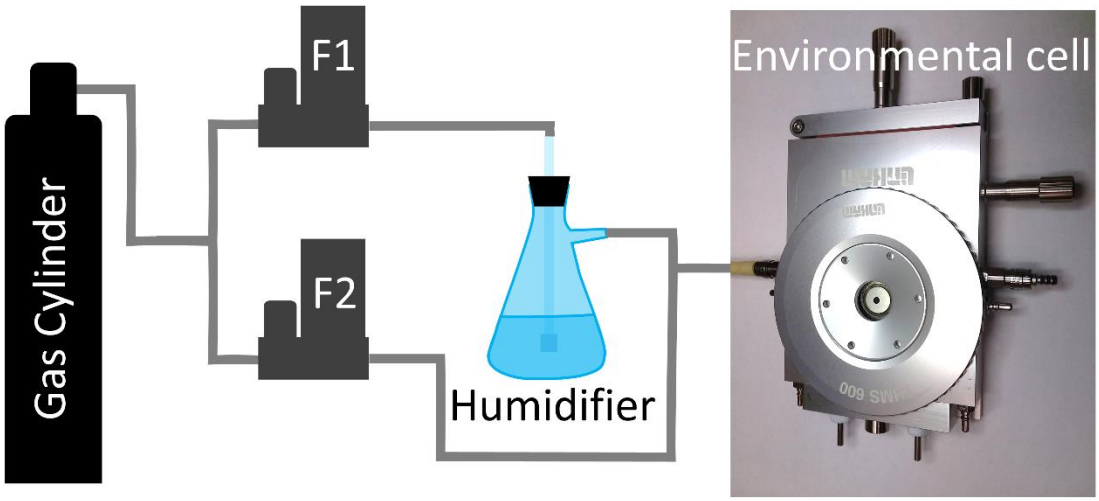

Figure S7. Schematic of the humidity-dependent optical measurements. Flow meters F1 and F2 control the flows of humid and dry gas. Both flows are mixed and sent to the environmental cell.

Electrochemical delamination

Before SEM studies, the electrochemical delamination tests have been conducted using a planar electrochemical cell equipped with two Pt electrodes and filled with 20% w/v PEGDA in PBS solution

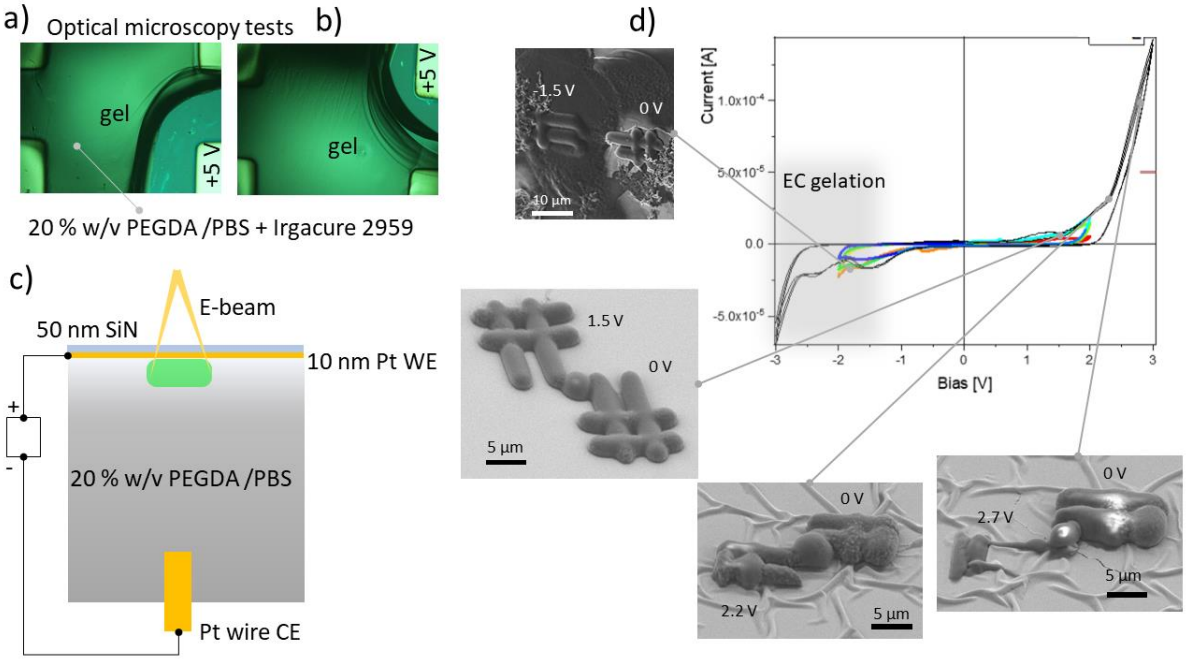

Figure S8. The effect of EC on beam-induced in-liquid PEGDA crosslinking. a), b) UV curing of PEGDA with anodic potential applied to different electrodes; c) The setup for electrochemical control of the e-beam induced crosslinking; C-V curves for Pt-Pt electrodes in 20% w/v PEGDA in PBS and SEM images of the log-pile strictures printed under selected biases.

doped with Irgacure 2959 initiator. The anodic potential at the working electrode was set close to the onset of water splitting reaction but to avoid bubbles formation. Under these conditions, the cell was irradiated

with UV light to crosslink the polymer. After irradiation, the cell was rinsed in DI water and the gel was inspected with an optical microscope. Figure S8 a, b shows the results of two different experiments where anodic potential applied to different electrodes. As can be seen, gel formation has been inhibited at the anode under these conditions. Electrochemical delamination experiments have been conducted using 50 nm thick SiN membranes coated with 10 nm to 20 nm of Pt as working electrodes or doped Si membranes. PBS solution was used as an electrolyte. The measurements have been done using a two-electrode setup (Figure S8 c). Figure S8d depicts current-voltage curves for such an EC cell and SEM images of the standard log-pile structure written under specified EC potentials. Cathodic potential generally leads to parasitic gelation of PEGDA while anodic potential progressively quenches beam induced crosslinking and, therefore, can be used to modulate the size and adhesion of the structures.

References

1. Demers, H.; Poirier-Demers, N.; Couture, A. R.; Joly, D.; Guilmain, M.; de Jonge, N.; Drouin, D., Three-Dimensional Electron Microscopy Simulation with the Casino Monte Carlo Software. *Scanning* **2011,** *33*, 135-146.
2. Joy, D.; Luo, S., An Empirical Stopping Power Relationship for Low-Energy Electrons. *Scanning* **1989,** *11*, 176-180.
3. Wang, C.-H.; Liu, C.-J.; Wang, C.-L.; Hua, T.-E.; Obliosca, J. M.; Lee, K.; Hwu, Y.; Yang, C.-S.; Liu, R.-S.; Lin, H.-M.; Je, J.-H.; Margaritondo, G., Optimizing the Size and Surface Properties of Poly (ethylene Glycol) (PEG)–Gold Nanoparticles by Intense X-Ray Irradiation. *J. Phys. D: Appl. Phys.* **2008,** *41*, 195301.
4. Krsko, P.; Sukhishvili, S.; Mansfield, M.; Clancy, R.; Libera, M., Electron-Beam Surface-Patterned Poly (ethylene Glycol) Microhydrogels. *Langmuir* **2003,** *19*, 5618-5625.
5. Meyerbröker, N.; Zharnikov, M., Modification and Patterning of Nanometer-Thin Poly (ethylene Glycol) Films by Electron Irradiation. *ACS Appl. Mater. Interfaces* **2013,** *5*, 5129-5138.
6. Kohl, H.; Reimer, L., *Transmission Electron Microscopy: Physics of Image Formation*. Springer Science & Business Media: New York, 2008.
7. Hayat, M. A., *Principles and Techniques of Electron Microscopy. Biological Applications*. Edward Arnold: London, 1981.
8. Kennedy, E.; Nelson, E. M.; Tanaka, T.; Damiano, J.; Timp, G., Live Bacterial Physiology Visualized with 5 nm Resolution Using Scanning Transmission Electron Microscopy. *ACS Nano* **2016,** *10*, 2669-2677.
9. Hermannsdörfer, J.; Tinnemann, V.; Peckys, D. B.; de Jonge, N., The Effect of Electron Beam Irradiation in Environmental Scanning Transmission Electron Microscopy of Whole Cells in Liquid. *Microsc. Microanal.* **2016,** *22*, 656-665.
10. Foster, G.; Buckley, C.; Bennett, P.; Burge, R., Investigation of Radiation Damage to Biological Specimens at Water Window Wavelengths. *Rev. Sci. Instr.* **1992,** *63*, 599-600.
11. Gupta, T.; Schneider, N. M.; Park, J. H.; Steingart, D.; Ross, F. M., Spatially Dependent Dose Rate in Liquid Cell Transmission Electron Microscopy. *Nanoscale* **2018,** *10*, 7702-7710.
12. Schneider, N. M.; Norton, M. M.; Mendel, B. J.; Grogan, J. M.; Ross, F. M.; Bau, H. H., Electron–Water Interactions and Implications for Liquid Cell Electron Microscopy. *J. Phys. Chem. C* **2014,** *118*, 22373-22383.
13. Bäckström, S.; Benavente, J.; W. Berg, R.; Stibius, K.; S. Larsen, M.; Bohr, H.; Hélix-Nielsen, C., Tailoring Properties of Biocompatible PEG-Dma Hydrogels with UV Light. *Mater. Sci. Appl.* **2012,** *3*, 425-431.
14. Kusuma, V. A.; Roth, E. A.; Clafshenkel, W. P.; Klara, S. S.; Zhou, X.; Venna, S. R.; Albenze, E.; Luebke, D. R.; Mauter, M. S.; Koepsel, R. R.; Russell, A. J.; Hopkinson, D.; Nulwala, H. B., Crosslinked Poly(ethylene Oxide) Containing Siloxanes Fabricated through Thiol-Ene Photochemistry. *J. Polym. Sci., Part A: Polym. Chem.* **2015,** *53*, 1548-1557.